MNRAS 000, 1–11 (2018) Preprint 20 February 2024 Compiled using MNRAS LATEX style file v3.0

Statistical properties of substructures around Milky Way-sized haloes and their implications for the formation of stellar streams

Yu Morinaga,[1]★ Tomoaki Ishiyama,[2] Takanobu Kirihara[2] and Kazuki Kinjo[1]
[1]*Department of Applied and Cognitive Informatics, Chiba University, 1-33, Yayoi-cho, Inage-ku, Chiba 263-8522, Japan*
[2]*Institute of Management and Information Technologies, Chiba University, 1-33, Yayoi-cho, Inage-ku, Chiba 263-8522, Japan*

Accepted 2019 May 14. Received 2019 May 10; in original form 2019 January 15

ABSTRACT

Stellar streams originating in disrupted dwarf galaxies and star clusters are observed around the Milky Way and nearby galaxies. Such substructures are the important tracers that record how the host haloes have accreted progenitor galaxies. Based on the cosmological context, we investigate the relationship between structural properties of substructures such as length and thinness at $z = 0$, and orbits of their progenitors. We model stellar components of a large sample of substructures around Milky Way-sized haloes by combining semi-analytic models with a high-resolution cosmological N-body simulation. Using the Particle Tagging method, we embed stellar components in progenitor haloes and trace phase-space distributions of the substructures down to $z = 0$. We find that the length and thinness of substructures vary smoothly as the redshift when the host haloes accrete their progenitors. For substructures observed like streams at $z = 0$, a large part of the progenitors is accreted by their host haloes at redshift $0.5 \lesssim z \lesssim 2.5$. Substructures with progenitors out of this accretion redshift range are entirely or less disrupted by $z = 0$ and cannot be observed as streams. We also find that the distributions of length and thinness of substructures vary smoothly as pericentre and apocentre of the progenitors. Substructures observed like streams tend to have the specific range of $10\ \mathrm{kpc} \lesssim r_{\mathrm{peri}} \lesssim 100\ \mathrm{kpc}$ and $50\ \mathrm{kpc} \lesssim r_{\mathrm{apo}} \lesssim 300\ \mathrm{kpc}$.

Key words: galaxies: formation – galaxies: dwarf – galaxies: structure – methods: numerical

1 INTRODUCTION

The standard lambda cold dark matter (CDM) scenario predicts that galaxies are formed via hierarchical mergers of smaller objects over its lifetime (White & Rees 1978). As a consequence of this merger process, a large number of substructures such as dwarf galaxies and their tidally disrupted remnants including stellar streams are expected to exist around galaxies as fossil records of their accretion events.

Among many kinds of substructures, stellar streams bring especially important clues to investigate galaxy formation. Infalling dwarf galaxies and star clusters into their host galaxies are tidally perturbed, and their stellar components are stripped. These stripped stellar components are elongated and formed tidal tails approximately along the progenitor orbits and observed as structures like "stream" at present (Johnston, Hernquist & Bolte 1996).

Such streams are the important tracers that record how the host haloes accreted progenitor galaxies because characteristic structural properties of streams should be significantly sensitive to their progenitor orbits (e.g., Hozumi & Burkert 2015) and also environments of their host galaxies such as the shape of underlying gravitational potential and interactions with other substructures (e.g., Johnston et al. 1999; Łokas, Gajda & Kazantzidis 2013).

So far, a large number of observations have actually discovered substructures including the Sagittarius stream (e.g., Ibata, Gilmore & Irwin 1994; Ibata et al. 2001b; Majewski et al. 2003), Orphan stream (Grillmair 2006; Belokurov et al. 2007; Fardal et al. 2018; Koposov et al. 2019) around the Milky Way (MW), the Giant Southern Stream in the Andromeda galaxy (M31) (e.g., Ibata et al. 2001a) and many other substructures in nearby galaxies (e.g., Martínez-Delgado et al. 2008; McConnachie et al. 2009). Recent surveys such as the Sloan Digital Sky Survey (SDSS), the *Gaia* mission (Gaia Collaboration et al. 2016),

★ E-mail: aefa2627@chiba-u.jp

Dark Energy Survey (DES)(Dark Energy Survey Collaboration et al. 2016), Pan-Andromeda Archaeological Survey (PAndAS) (McConnachie et al. 2009; Martin et al. 2013), the Panoramic Survey Telescope and Rapid Response System (Pan-STARRS) (Kaiser et al. 2002) and Subaru Hyper Suprime-Cam (Miyazaki et al. 2006, 2012) have been discovering new faint dwarf galaxies and stellar streams, and measuring some properties of a part of individual stars (e.g., Kalirai et al. 2010; Richardson et al. 2011; Tollerud et al. 2012; Drlica-Wagner et al. 2015; Helmi et al. 2018; Simon 2018; Shipp et al. 2018; Komiyama et al. 2018; Fu et al. 2018; Homma et al. 2018). These past, ongoing and planning surveys would enable us to characterise the structural properties for plenty of substructures such as the length and thinness in more detail and infer the origin of substructures by comparing with some theoretical models.

To investigate the relationship between structural properties of streams, orbits of their progenitors and environments, various studies have been carried out (e.g., Ibata et al. 2001b; Johnston, Sackett & Bullock 2001; Johnston et al. 2008; Majewski et al. 2003; Peñarrubia, McConnachie & Babul 2006; Peñarrubia et al. 2010; Fardal et al. 2007, 2008, 2013; Sales et al. 2007, 2008; Martínez-Delgado et al. 2008; Varghese, Ibata & Lewis 2011; Carlberg 2012; Foster et al. 2014; Miki et al. 2014; Miki, Mori & Rich 2016; Sandford et al. 2017; Kirihara et al. 2017; Kirihara, Miki & Mori 2017; Bonaca & Hogg 2018). Ibata et al. (2001b) suggested that the gravitational potential of the MW must be nearly spherical to reproduce the observed positions and velocities of stars in the Sagittarius stream. A few gaps found along stellar streams may be caused by a large population of low-mass subhaloes predicted by the CDM model (Carlberg 2012; Ibata, Lewis & Martin 2016; Sandford et al. 2017), which may be a possible explanation for the so called "missing satellite" problem (Klypin et al. 1999; Moore et al. 1999).

For these studies, N-body simulations have been extensively used to reproduce observed properties of substructures and to explore the dynamical evolution of them. In many earlier studies, fixed and spherical gravitational potential of host galaxies is assumed, and orbits of satellite galaxies are free parameters. However, in the cosmological context, dynamical evolution of substructures are significantly affected by complicated physics such as dynamical friction, multiple interactions with other subhaloes, and evolutionary history of host galaxies, which could not be treated in fixed gravitational potential. Orbital parameters of infalling satellites have some specific distributions (Wetzel 2011). Consequently, tracing the dynamical evolution of substructures using N-body simulations in simple galactic models is insufficient to estimate their origins precisely. Studies based on the cosmological context are highly demanded.

Diemand, Kuhlen & Madau (2007) analysed co-evolution of abundant subhaloes with a host halo formed in their cosmological N-body simulation and showed the mass evolution of subhaloes depends on orbital properties such as pericentre. Warnick, Knebe & Power (2008) examined the formation and evolution of tidal streams originated in cosmological disrupted subhaloes and found correlations between the structures of streams and some properties of progenitor haloes such as infalling masses and orbital parameters. However, the dynamical evolution of subhaloes and dwarf galaxies differ because tidal stripping preferentially occurs in the outer part of haloes. Besides, they used only one MW-sized host halo, which is not enough to capture the statistics of structural properties of substructures.

To shed light on these issues, we explore the dynamical evolution and structural properties of stellar components of a large sample of substructures within the cosmological context. In particular, we focus on substructures originating in "dwarf galaxies", while Carlberg (2018b,a) have explored the formation and evolution of streams originating in globular clusters and their density gaps. We combine a high-resolution cosmological N-body simulation (Ishiyama et al. 2016) with the "Particle Tagging" method to embed stellar components into haloes, which has succeeded to reproduce some observed features of the stellar halo of the MW (e.g., De Lucia & Helmi 2008). Cooper et al. (2010) have developed an extension method of the Particle Tagging, which is also used to study stellar streams near solar neighbourhood (Gómez et al. 2013). To assign stellar masses to haloes, we use a simple model proposed by Koposov et al. (2009). We aim to investigate the relationship between structural properties of substructures such as length and thinness at $z = 0$, and the orbits of their progenitors in MW-sized haloes.

This paper is organised as follows. In Section 2, we describe the details of our cosmological N-body simulation. In Section 3, we explain the analytic models and the definition of structural and orbital properties of substructures. In Section 4, we show the results of our statistical analysis of substructures. Finally, we discuss and summarise our results in Section 5.

2 COSMOLOGICAL N-BODY SIMULATION

We used a high-resolution cosmological N-body simulation conducted by Ishiyama et al. (2016). This simulation consists of 2048^3 dark matter particles in an 11.8 Mpc comoving cubic box. The particle mass is $7.54 \times 10^3 M_\odot$, and the gravitational softening length is ε =176.5 pc. The cosmological parameters are consistent with the observation of the cosmic microwave background obtained by the Planck satellite (Planck Collaboration et al. 2014, 2018), namely, $\Omega_0 = 0.31, \Omega_b = 0.048, \lambda_0 = 0.69, h = 0.68, n = 0.96$, and $\sigma_8 = 0.83$. The snapshots were stored at the redshifts so that the logarithmic interval $\Delta\log(1+z) = 0.01$. We identified dark matter haloes and subhaloes using ROCKSTAR (Robust Overdensity Calculation using K-Space Topologically Adaptive Refinement) halo/subhalo finder (Behroozi, Wechsler & Wu 2013). Then we constructed their merger trees using CONSISTENT TREE code (Behroozi et al. 2013), Further details of this simulation are given in Ishiyama et al. (2016).

In this study, we analysed nine MW-sized haloes (GX1-GX9). Their virial mass is between $0.55 - 2.84 \times 10^{12} M_\odot$, where the definition of virial mass is given by Bryan & Norman (1998). Their properties such as the virial mass $M_{\rm vir}$ and the virial radius $R_{\rm vir}$ are summarised in Table 1. From their merger trees, we selected progenitor haloes with masses more massive than $M_{\rm vir} > 10^7 M_\odot$ at redshift $z_{\rm acc}$ when they first pass through the virial radius of the most massive progenitors of MW-sized haloes (so-called "main-branch"). Then, we traced the evolution of these haloes after the redshift

$z_{\rm acc}$. The number of subhaloes in each host halo is listed in Table 1.

After the redshift $z_{\rm acc}$, most progenitor haloes orbit host haloes as subhaloes. Some of them are disrupted by the gravitational interaction with the host haloes and cannot be observed at $z = 0$ as subhaloes in the merger tree. In the following section, we tag a part of member particles of subhaloes at $z_{\rm acc}$ using the "Particle Tagging" method and regard these particles as the stellar component. By tracing these stellar particles down to $z = 0$, we can analyse the phase space distributions of both surviving and disrupted "galaxies" at $z = 0$. Hereafter, including streams, we refer to these objects as "substructures". In Section 3.4, we categorise them by length and thinness of substructures at $z = 0$ into three types, self-bounded subhalo, stream and disrupted substructure. Because there is no consensual and rigid definition of them from the viewpoint of observations, we refer to substrcutures using these three terms as a matter of convenience.

3 METHODS

3.1 Particle Tagging

Adopting the "Particle Tagging" method (e.g., Bullock, Kravtsov & Weinberg 2001; Diemand, Madau & Moore 2005; Bullock & Johnston 2005; De Lucia & Helmi 2008; Cooper et al. 2010) to dark matter only simulations, we can embed stellar components in progenitor haloes and trace their phase space distributions down to $z = 0$. Most stellar components are assumed to be formed in the centre of progenitor haloes until the redshift $z_{\rm acc}$ when they first pass through the virial radius of their host haloes. We tag a fixed fraction of $f_{\rm MB}$ of the most bound particles of those progenitors at $z_{\rm acc}$,[1] and treat these particles as "stellar particles". Tracing these particles down to $z = 0$, we can investigate the phase space distributions of substructures originating in progenitor haloes. We set $f_{\rm MB} = 0.10$ by default.

The similar approach was adopted by De Lucia & Helmi (2008). They also used $f_{\rm MB} = 0.10$ and showed that physical properties such as the metallicity and the age of stars in accreted stellar haloes of their model galaxies were good agreement with the observed data. Besides, they found that observed structural properties of the stellar component around the MW were well reproduced, reinforcing the effectiveness of the Particle Tagging method. Cooper et al. (2010) have also developed an extension of this method, which is confirmed to be able to provide an excellent approximation to hydrodynamical simulations (Cooper et al. 2017).

In our study, combining the Particle Tagging method with the higher resolution cosmological N-body simulation described in Section 2, we can resolve substructures such as streams originating in smaller haloes and investigate structural properties of them. Although we used the fraction $f_{\rm MB} = 0.10$ as a fiducial value, we also compared the results with $f_{\rm MB} = 0.05$ and 0.20, and confirmed that the differences in $f_{\rm MB}$ do not strongly affect statistical results of the relationship between structural properties of substructures and orbits of their progenitors. The detail is given in Appendix A.

[1] If the progenitor halo is a "phantom" halo (Behroozi, Wechsler & Wu 2013) in the merger tree at $z_{\rm acc}$, we trace the progenitor back to redshift when it is not phantom and perform the tagging.

3.2 A model to assign stellar masses to haloes

In cosmological N-body simulations, MW-sized haloes contain a number of subhaloes as listed in Table 1. However, the number of known dwarf galaxies in the MW and M31 is two or three dozens (McConnachie 2012). This disagreement is known as the so-called "missing satellite" problem (Klypin et al. 1999; Moore et al. 1999). To investigate the statistical properties of visible substructures, it is necessary to assign stellar masses to progenitor haloes in a physically motivated manner.

Photoionising by the cosmic UV background radiation sufficiently suppresses the star formation in low-mass haloes with the viral temperatures $T_{\rm vir} < 10^4$ K. Such haloes unable to cool the gas and form stars even if sufficient amount of gas exists (Haiman, Rees & Loeb 1997). To assign stellar masses to subhaloes, we used a model based on this picture proposed by Koposov et al. (2009) that reproduces the distribution of dwarf galaxies observed by the Sloan Digital Sky Survey.

In this model, when the circular velocity of a progenitor halo $V_{\rm circ}$ at the reionization epoch $z_{\rm rei} \sim 11$ (e.g., Dunkley et al. 2009) is above a critical threshold $V_{\rm crit,r} \sim 10$ km s^{-1} (corresponding to $T_{\rm vir} \sim 10^4$ K), the stellar mass of the progenitor halo is given by Equation (1)

$$M_* = \frac{f_*(M_{\rm sat}-M_{\rm rei})}{(1+0.26(V_{\rm crit}/V_{\rm circ}(z_{\rm acc}))^3)^3} + f_* M_{\rm rei} \quad (V_{\rm circ}(z_{\rm rei}) > V_{\rm crit,r}), \qquad (1)$$

where $M_{\rm sat}$ and $M_{\rm rei}$ are the virial masses of the progenitor halo at $z_{\rm acc}$ and $z_{\rm rei}$, respectively, and the stellar mass fraction is $f_* = 10^{-3} \times \Omega_0/\Omega_{\rm b}$. In this case, it is assumed that such halo is massive enough to form stars in the pre-reionization era. On the other hand, for a progenitor halo with $V_{\rm circ}(z_{\rm rei}) < V_{\rm crit,r}$, the stellar mass is assigned by Equation (2), assuming very low star formation efficiency in the pre-reionization era,

$$M_* = \frac{f_* M_{\rm sat}}{(1 + 0.26(V_{\rm crit}/V_{\rm circ}(z_{\rm acc}))^3)^3} \quad (V_{\rm circ}(z_{\rm rei}) < V_{\rm crit,r}). \qquad (2)$$

In these equations, the suppression of star formation occurs for haloes with the circular velocity below a critical value $V_{\rm crit}$ after the reionization, based on cosmological hydrodynamical simulations (e.g., Gnedin 2000; Hoeft et al. 2006; Okamoto, Gao & Theuns 2008) , and thus resulting stellar masses are significantly affected by the choice of $V_{\rm crit}$. Gnedin (2000) proposed the critical circular velocity $V_{\rm crit} \sim 40$ km s^{-1}, but lower critical values $V_{\rm crit} \sim 20 - 25$ km s^{-1} were suggested by Hoeft et al. (2006) and Okamoto, Gao & Theuns (2008). We vary $V_{\rm crit}$ and select an appropriate value so that the observed stellar mass function of dwarf galaxies is reproduced well.

Figure 1 shows the cumulative number of subhaloes at $z = 0$ (not substructures) in nine MW-sized host haloes (GX1-GX9) as a function of stellar mass, for models of $V_{\rm crit} = 20, 30$ and 40 km s^{-1}. Filled and open symbols are the distributions of the observed dwarf galaxies in the MW and M31 (McConnachie 2012), respectively. Koposov et al. (2009) adopted this model and successfully reproduced the distribution of the observed stellar mass function of dwarf

Table 1. Properties of nine Milky-Way sized haloes. $M_{\rm vir}$ and $R_{\rm vir}$ are the virial mass and radius. $N_{\rm sub}$ is the number of subhaloes with $M_{\rm vir}(z_{\rm acc}) > 10^7 M_\odot$, where $z_{\rm acc}$ is the redshift when progenitors of substructures first pass through the virial radius of the most massive progenitors of their MW-sized host haloes. $N_{{\rm sub},M_*=10^{4-5}}$, $N_{{\rm sub},M_*=10^{5-6}}$ and $N_{{\rm sub},M_*>10^6}$ are the number of substructures whose stellar mass ranges are $M_* = 10^{4-5}$, 10^{5-6} and $10^{6-} M_\odot$, respectively. The numbers in the brackets are those of the streams with each stellar mass ranges.

Name	$M_{\rm vir}$ [$\times 10^{12} M_\odot$]	$R_{\rm vir}$ [kpc]	$N_{\rm sub}$	$N_{{\rm sub},M_*=10^{4-5}}$	$N_{{\rm sub},M_*=10^{5-6}}$	$N_{{\rm sub},M_*>10^6}$
GX1	2.84	372	6560	158 (16)	52 (8)	18 (2)
GX2	2.36	350	4956	104 (23)	48 (8)	20 (2)
GX3	2.27	345	3810	86 (11)	20 (2)	14 (2)
GX4	1.09	270	2421	69 (6)	19 (0)	9 (1)
GX5	0.74	238	1853	32 (7)	20 (5)	7 (0)
GX6	0.45	201	959	17 (0)	11 (0)	5 (0)
GX7	0.59	221	1135	35 (2)	8 (1)	6 (0)
GX8	0.60	222	1421	26 (2)	11 (3)	9 (0)
GX9	0.55	216	1016	26 (1)	11 (0)	3 (0)

galaxies excluding Large/Small Magellanic Clouds. In the same manner, we also plot the stellar mass function of the MW and M31 excluding the Magellanic Clouds, M33 and M32.

Subhaloes with lower stellar masses ($M_* < 10^4 M_\odot$) are more abundant than observed dwarf galaxies of both the MW and M31 regardless of $V_{\rm crit}$. One of the reasons is that it is hard to observe such ultra faint dwarf galaxies due to the detection limit. However a part of such faint dwarf galaxies would be discovered by ongoing deep imaging surveys by Subaru Hyper Suprime-Cam (e.g. Homma et al. 2016, 2018). Another reason is that the suppression of star formation in low-mass haloes might be insufficient in this model. Because such dwarf galaxies are too faint, we only analyse substructures with $M_* > 10^4 M_\odot$ in this study. Thus, this disagreement of the number of low stellar mass dwarf galaxies does not change our conclusion.

Although subhaloes with the stellar mass $M_* > 10^8 M_\odot$ are not found in any host haloes in our simulation, such satellites are observed in the MW and M31 such as Large/Small Magellanic Clouds, M33 and M32. Recent cosmological simulations have also shown that MW-sized haloes to host such massive satellites are rare (Boylan-Kolchin, Besla & Hernquist 2011; Busha et al. 2010). Therefore, this disagreement does not affect the statistical properties of substructures. When we exclude these dwarf galaxies, the agreement between our model and the observation becomes better for $V_{\rm crit} = 20$ and 30 km s^{-1}. Hereafter, we use $V_{\rm crit} = 30$ km s^{-1}, and the number of substructures (not subhaloes at $z = 0$) with the critical threshold $V_{\rm crit} = 30$ km s^{-1} in each host halo is listed in Table 1.

3.3 Orbital parameters

To analyse orbital histories of subhaloes and how they relate to the properties of substructures, we quantify the pericentre and apocentre of subhaloes. Wetzel (2011) explored orbital properties of infalling satellites and reported their dependence on the host and satellite masses and redshift. They calculated the orbital circularity and pericentre by the two-body approximation (host and satellite haloes). This procedure would be valid for infalling satellites. However, after $z_{\rm acc}$, actual orbital properties such as pericentre and apocentre evolve via dynamical friction, tidal disruption, and multiple interactions between subhaloes. Therefore, the two-body approximation is not accurate enough to describe the orbital properties.

To calculate the pericentre and apocentre of subhaloes more accurately, we trace their orbits from $z_{\rm acc}$ to $z = 0$ or the redshift when they are entirely merged with their host haloes. Then we define the pericentre (apocentre) as the smallest value in local minima (maxima) of the radial distance of subhaloes. When subhaloes do not experience any pericentre or apocentre passages, we define the pericentre as the smallest radial distance and the apocentre as the largest radial distance after $z_{\rm acc}$ so that we can quantify the orbital properties.

3.4 Quantifying structural properties of substructures

We characterise structural properties of substructures at $z = 0$ and explore the relationship between them and the orbits of progenitors. We quantify them with two characteristic parameters, length $L_{\rm sub}$, and thinness $T_{\rm sub}$.

3.4.1 Definition of the length of substructures $L_{\rm sub}$

We define the length of substructures as follows. At first, we perform the Principal Component Analysis (PCA) for the stellar particles of substructures in the three-dimensional coordinate. The spatial coordinate is transformed to the new coordinate (PC1-3). Then, we define the length of a substructure $L_{\rm sub}$ as the sum of physical distances of two stellar particles that lie furthest along the PC1 axis to the centre of the substructure. To exclude outliers, we count the number of stellar particles in the substructure along the PC1 axis at intervals of 15ε ($= 15 \times 176.5$ pc) and remove particles in the region whose number of particles is below five in calculating the length. In this case, the threshold of the outlier removal step is represented by $\rho_{N_{\rm p}} = 5$. Although we use $\rho_{N_{\rm p}} = 5$ as a fiducial value throughout this paper, we also compare the results of the structural properties of substructures with $\rho_{N_{\rm p}} = 0$ and 25 in Appendix B, which indicates that statistical results are insensitive to the choice of $\rho_{N_{\rm p}}$.

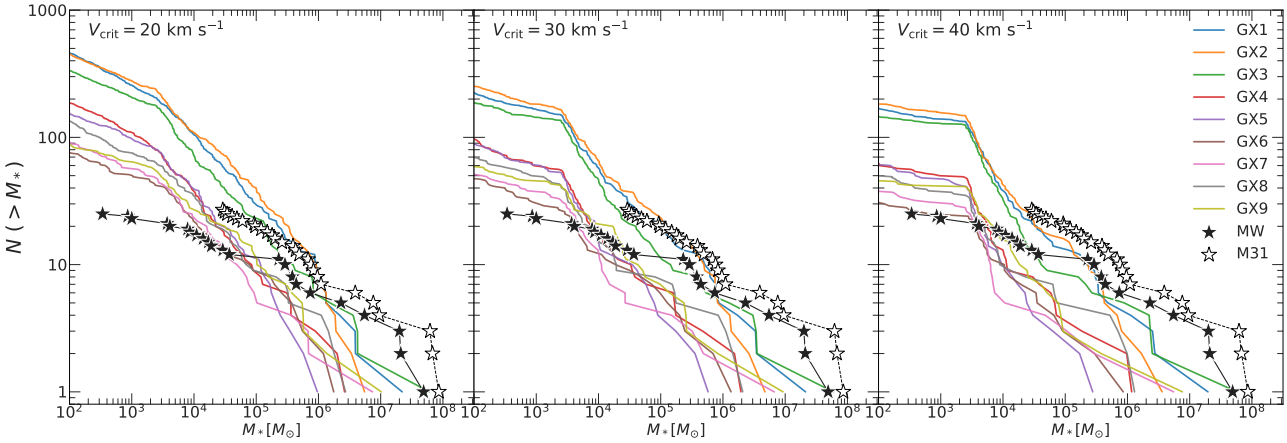

Figure 1. Cumulative number of subhaloes at $z = 0$ in nine MW-sized host haloes (GX1-GX9) as a function of their stellar mass, for models with $V_{\rm crit} = 20, 30$ and 40 km s^{-1}. Filled and open symbols are respectively those of the observed dwarf galaxies in the MW and M31, (McConnachie 2012), and the stellar masses are derived from absolute visual magnitude assuming a stellar-to-light ratio of one. The data of Large/Small Magellanic Clouds, M33 and M32 are excluded.

3.4.2 Definition of the thinness of substructures $T_{\rm sub}$

To quantify the thinness of substructures, we apply a similar method proposed by Sandford et al. (2017). We perform PCA for the stellar particles of substructures in the three-dimensional coordinate, and each stellar particle (denoted by i) is represented by principal components scores $t_{k(i)} (k = 1, 2, 3)$. The PC1 (PC3) scores have the largest (smallest) variance in the three.

Using these variances, we define the thinness $T_{\rm sub}$ as

$$T_{\rm sub} = \sqrt{\frac{\sum_{i=1}^{N_{\rm p}} \left(\mathbf{t}_{1(i)} - \overline{\mathbf{t}_1}\right)^2}{\sum_{i=1}^{N_{\rm p}} \left(\mathbf{t}_{3(i)} - \overline{\mathbf{t}_3}\right)^2}} \quad , \tag{3}$$

where $N_{\rm p}$ is the number of stellar particles in the substructure. In other words, $T_{\rm sub}$ represents the ratio of the standard deviation of PC1 to PC3. For example, a substructure with high-$T_{\rm sub}$ is elongated along PC1 and would be observed like a stream at $z = 0$. On the other hand, a substructure with low-$T_{\rm sub}$ (~ 1) distributes three-dimensionally, which means it is entirely disrupted or is not much tidally affected.

3.4.3 Definition of the stream

We consider that substructures with large values of the length and thinness can be observed as stellar streams. In this paper, we refer to substructures with $L_{\rm sub}/R_{\rm vir} > 5$ and $T_{\rm sub} > 6$ at $z = 0$ as streams, where $R_{\rm vir}$ is the virial radius of the progenitor halo at $z_{\rm acc}$. In the case of massive substructures, $L_{\rm sub}$ is naturally high even if they are not tidally disrupted. To pick up tidally elongated substructures, we define the stream by $L_{\rm sub}/R_{\rm vir}$, which represents the relative disruption of substructures. Entirely disrupted substructures or slightly disrupted substructures are not categorised as streams in this definition because such substructures have smaller values of $T_{\rm sub}$.

4 RESULTS

4.1 Distribution of length $L_{\rm sub}$ and thinness $T_{\rm sub}$

Figure 2 shows the distributions of length and thinness of all substructures with stellar mass ranges of $M_* = 10^{4-5}, 10^{5-6}$ and $10^{6-} M_\odot$ in nine MW-sized haloes (GX1-GX9). The distribution of the length shows a bimodality regardless of the stellar mass range. The first peak at short length around 10 kpc originates from less disrupted substructures. The second peak at the long length from 100 to 200 kpc originates from entirely disrupted substructures. The first peak slightly shifts towards the long length with increasing the stellar mass because the size of progenitor haloes becomes larger. On the other hand, the second peak is almost unchanged.

The distribution of thinness shows that the number of substructures decreases as the thinness increases, and peaks at around 1. This trend is also seen in substructures with any stellar mass ranges, indicating that the highly elongated substructures are quite rare and a large part of substructures is not observed as streams at $z = 0$.

4.2 Relation between length $L_{\rm sub}$, thinness $T_{\rm sub}$ and accretion redshift $z_{\rm acc}$

To explore the accretion histories of substructures around MW-sized haloes at $z = 0$, we plot the distributions of $z_{\rm acc}$ and masses of their progenitor haloes $M_{\rm vir}(z_{\rm acc})$ at $z_{\rm acc}$ in Figure 3. From the overall distribution of $z_{\rm acc}$, the number of progenitors with mass $M_{\rm vir}(z_{\rm acc}) > 10^7 M_\odot$ tends to be decreasing with increasing redshift from $z = 4$, just because haloes more massive than this value are not enough formed (the half mass formation epoch of such haloes is $z < 3$ (Ishiyama et al. 2015)). These trends propagate substructures with the stellar mass $M_* > 10^4 M_\odot$. The distributions of streams are clearly different from the overall distribution of substructures. A large part (approximately 90%) of the streams is accreted by their host haloes within $0.5 \lesssim z_{\rm acc} \lesssim 2.5$. On the other hand, only 20% of all substructures is accreted within this redshift range.

As shown in the bottom panel of Figure 3, the mass

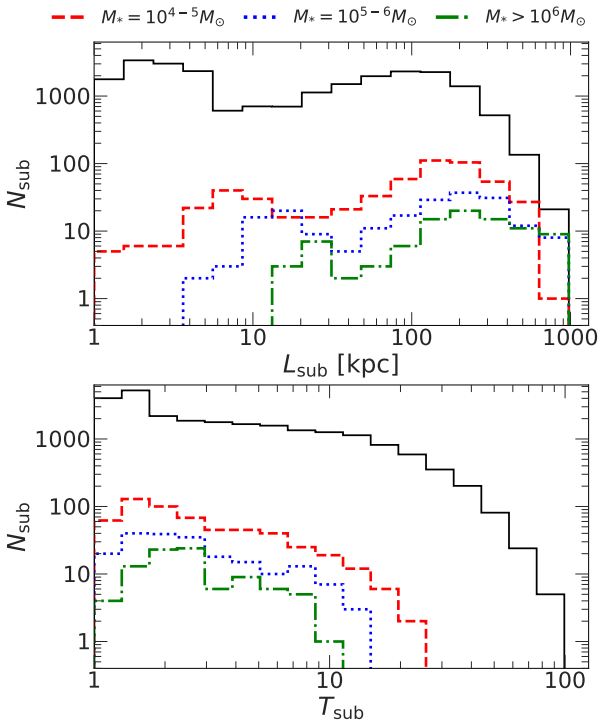

Figure 2. Distribution of length $L_{\rm sub}$ (top panel) and thinness $T_{\rm sub}$ (bottom panel) of all substructures in nine MW-sized haloes (GX1-GX9) at $z = 0$. Red dashed, blue doted and green dash-dotted curves show the results of substructures with the stellar mass ranges of $M_* = 10^{4-5}, 10^{5-6}$ and $10^{6-} M_\odot$, respectively. Solid curves show the distribution of substructures with $M_{\rm vir}(z_{\rm acc}) > 10^7\ M_\odot$.

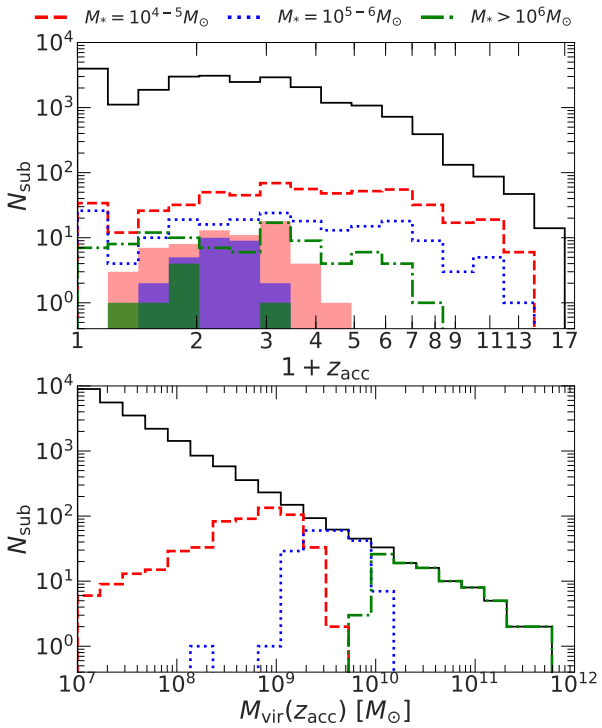

Figure 3. Top: Histograms of $z_{\rm acc}$, when progenitors of substructures first pass through the virial radius of the most massive progenitors of their MW-sized host haloes. Bottom: Histograms of the virial mass of progenitors of substructures $M_{\rm vir}(z_{\rm acc})$ at $z_{\rm acc}$. Dashed curves show the distribution of substructures with the stellar mass ranges of $M_* = 10^{4-5}, 10^{5-6}$ and $10^{6-} M_\odot$, respectively. Solid curves show the distribution of substructures with $M_{\rm vir}(z_{\rm acc}) > 10^7\ M_\odot$. In the upper panel, the filled histograms show the distributions of $z_{\rm acc}$ of streams, which are defined in §3.4.3.

distribution of substructures with the progenitor mass $M_{\rm vir}(z_{\rm acc}) > 10^7 M_\odot$ approximately follows a power law. However, those within a certain range of stellar masses differ depending on the range. The substructures with the stellar mass ranges of $M_* = 10^{4-5}, 10^{5-6}$ and $10^{6-} M_\odot$ approximately correspond to the progenitor haloes with the mass ranges of $M_{\rm vir}(z_{\rm acc}) = 10^{7-9}, 10^{9-10}$ and $10^{10-} M_\odot$, respectively. Almost all the progenitor haloes with mass $M_{\rm vir}(z_{\rm acc}) \gtrsim 10^9 M_\odot$ have relatively massive stellar components ($M_* > 10^5 M_\odot$). On the other hand, in low-mass progenitor haloes, the star formation is strongly suppressed in our model due to the photoionised heating by the cosmic UV background radiation. Therefore, a large part of low-mass progenitor haloes with the mass below $10^8 M_\odot$ at $z_{\rm acc}$ is excluded in our analysis.

Figure 4 shows the distributions of length and thinness at $z = 0$ for substructures with the stellar mass ranges of $M_* = 10^{4-5}, 10^{5-6}$ and $10^{6-} M_\odot$. The length tends to get longer, and the thinness tends to get slightly smaller for substructures with more stellar masses as shown in Figure 2. The length and thinness vary smoothly as the accretion redshift $z_{\rm acc}$. A large part of substructures with $z_{\rm acc} \lesssim 0.5$ exists in the region with the short length ($L_{\rm sub} \sim 10$ kpc) and the small thinness ($T_{\rm sub} \sim 1$), indicating that these substructures are less affected by tidal forces from their host haloes because of recent accretion (small $z_{\rm acc}$). On the other hand, a large part of substructures with $z_{\rm acc} \gtrsim 0.5$ is strongly perturbed by the tidal force and has the long length. The typical length of substructures at $z_{\rm acc}$ is about 1-10 kpc, increased by a factor of approximately 1-50 until $z = 0$. These substructures show a clear correlation between $T_{\rm sub}$ and $z_{\rm acc}$. The thinness is decreasing with increasing $z_{\rm acc}$. In particular, substructures with the long length ($L_{\rm sub} \gtrsim 100$ kpc) and the large thinness ($T_{\rm sub} \gtrsim 6$), which are defined as streams in this work, give a specific redshift range of $0.5 \lesssim z_{\rm acc} \lesssim 2.5$ as shown in Figure 3.

Toward higher accretion redshift ($z_{\rm acc} \gtrsim 2.5$), the thinness of substructures tend to become gradually smaller in any stellar mass ranges. These substructures suffer from strong tidal forces, can be entirely disrupted by $z = 0$ and cannot be observed as streams. These trends are highlighted in Figure 5, which shows the distributions of stellar particles of substructures with different accretion redshift ranges of $z_{\rm acc} < 0.5$, $0.5 < z_{\rm acc} < 2.5$ and $z_{\rm acc} > 2.5$. This figure visualises that the different accretion redshift gives the stark difference in structural properties of substructures.

Substructures with the accretion redshift $z_{\rm acc} < 0.5$ are less disrupted, and their stellar particles distribute compactly. Thus, their length and thinness tend to be short and small at $z = 0$. In the case of substructures with $z_{\rm acc} > 2.5$, most of them are entirely disrupted, and their stellar particles are scattered vastly at $z = 0$. As a consequence, their length stays long, and thinness tends to become smaller with increasing accretion redshift. On the other hand, substruc-

tures with characteristic accretion redshift $0.5 < z_{\rm acc} < 2.5$ show a variety of structures at $z = 0$. Some of them are largely disrupted and formed stream-like structures. Additionally, there are also some substructures that are less or entirely disrupted. Therefore, these substructures with the characteristic accretion redshift show some scatters in Figure 4. These scatters can also be resulted from the variation of orbital properties of their progenitor haloes.

4.3 Relation between length, thinness and orbital parameters

In this section, we investigate the relation between the properties of substructures and orbital parameters. Figure 6 shows the distributions of pericentre $r_{\rm peri}$ and apocentre $r_{\rm apo}$ for progenitors of substructures and streams with the stellar mass ranges of $M_* = 10^{4-5}, 10^{5-6}$ and $10^{6-}M_\odot$.

The distribution of the pericentre of substructures with $M_{\rm vir}(z_{\rm acc}) > 10^7 M_\odot$ peaks at around $r_{\rm peri} \sim 30$ kpc, implying that the progenitor haloes with smaller $r_{\rm peri}$ tend to be entirely merged with their host haloes by $z = 0$. This peak is also seen in the substructures with the stellar mass of $M_* > 10^4 M_\odot$, however, is less prominent. The progenitor haloes experience pericentre passages in a rather wide range of $r_{\rm peri} \lesssim 300$ kpc. On the other hand, a large part of progenitor haloes of streams experiences pericentre passages in a shorter and narrow range of 10 kpc $\lesssim r_{\rm peri} \lesssim 100$ kpc, and the peak is more prominent.

The number of substructures with $M_{\rm vir}(z_{\rm acc}) > 10^7 M_\odot$ increases with increasing apocentre. This dependence is weakened in the substructures with stellar mass of $M_* > 10^4 M_\odot$. It means that numerous lower stellar mass haloes are just infalling into the host haloes. On the other hand, the apocentre of a large part of streams distributes in $r_{\rm apo} \gtrsim 50$ kpc. The distributions of pericentre and apocentre of streams show the stark difference from the overall distribution of substructures.

To see the relation between the properties of substructures and the orbital parameters, we plot the distribution of length versus thinness as functions of orbital parameters for substructures with stellar mass ranges of $M_* = 10^{4-5}, 10^{5-6}$ and $10^{6-}M_\odot$ in Figure 7. As well as the distribution of $z_{\rm acc}$ shown in Figure 4, the distributions of the length and thinness vary smoothly as the pericentre and apocentre in any stellar mass ranges.

Substructures whose progenitor haloes have larger pericentre ($\gtrsim 100$ kpc) tend to exist in the rather narrow region of length and thinness plane ($L_{\rm sub} \sim 10$ kpc and $T_{\rm sub} \sim 1$). These substructures are less tidally disrupted by host haloes until $z = 0$, corresponding to substructures with lower $z_{\rm acc}$. On the other hand, a large part of substructures with smaller pericentre ($\lesssim 100$ kpc) is strongly perturbed by tidal forces of host haloes, gets their length longer, and shows a considerable variation of thinness. Notably, the substructures observed like streams tend to originate in progenitor haloes with a specific range of pericentre of 10 kpc $\lesssim r_{\rm peri} \lesssim 100$ kpc, corresponding to the substructures with $0.5 \lesssim z_{\rm acc} \lesssim 2.5$ as shown in Figure 4.

For substructures with smaller pericentre ($\lesssim 10$ kpc), their thinness becomes smaller with decreasing pericentre although there is some scatter. These results suggest that progenitor haloes of such substructures experience multiple pericentre passages and are entirely disrupted or make multiple streams because their accretion redshift tends to be higher than $z = 2.5$ as shown in Figure 4. The higher $z_{\rm acc}$ means that the size of host haloes at $z_{\rm acc}$ is smaller than their counterparts at $z = 0$ and orbital decay due to dynamical friction acts more effectively, contributing the smaller pericentre.

These overall trends are common in any stellar mass ranges, and similar trends are also seen in the distribution of length versus thinness as a function of apocentre. Substructures observed like streams tend to have apocentre above 100–200 kpc, which is slightly smaller than the value that less disrupted substructures have ($L_{\rm sub} \sim 10$ kpc and $T_{\rm sub} \sim 1$).

Figure 8 gives another look of the relation between the properties of substructures and the orbital parameters, which is the pericentre versus apocentre as a function of length and thinness. The pericentre and apocentre of progenitor haloes distribute in wide ranges from a few to 300 kpc and correlate with each other. As also seen in Figure 7, the distributions of length and thinness of substructures vary as pericentre and apocentre. It is clear that substructures observed like streams are concentrated in the narrow region of the pericentre and apocentre plane of 10 kpc $\lesssim r_{\rm peri} \lesssim$ 100 kpc and 50 kpc $\lesssim r_{\rm apo} \lesssim 300$ kpc. These trends are shown in any stellar mass ranges.

From these results, we can infer the evolution of structural properties of substructures in terms of the accretion redshift and the orbital parameters. We can clearly see that moderate tidal effects from host haloes are necessary to form streams. Substructures with higher accretion redshift ($z_{\rm acc} > 2.5$) suffer from strong tidal forces and orbital decay, or have smaller host haloes at $z_{\rm acc}$, resulting in smaller pericentre and apocentre. Such substructures experience multiple pericentre passages and are entirely disrupted or make multiple streams, making length longer and thinness smaller. Substructures with lower accretion redshift ($z_{\rm acc} < 0.5$) are less affected by the tidal forces and keep larger pericentre and apocentre until $z = 0$, and also keep their gravitationally bound structures.

5 DISCUSSIONS AND SUMMARY

In this study, we have investigated the relationship between structural properties of substructures and orbits of their progenitors around MW-sized haloes. Using a high-resolution cosmological N-body simulation and the Particle Tagging method, we have explored the dynamical evolution of a large sample of substructures based on cosmological context more precisely than previous similar studies using N-body simulations and simple galactic models.

We have characterised structural properties of substructures using two quantities, length $L_{\rm sub}$ and thinness $T_{\rm sub}$, and have found that both quantities at $z = 0$ vary smoothly as accretion redshift $z_{\rm acc}$ when their progenitor haloes are accreted onto the host haloes. In the case of substructures with $z_{\rm acc} < 0.5$, their length and thinness tend to be short and small ($L_{\rm sub} \sim 10$ kpc and $T_{\rm sub} \sim 1$). On the other hand, a large part of substructures (approximately 90%) observed like "streams" at $z = 0$ is accreted at the specific accretion redshift range $0.5 \lesssim z_{\rm acc} \lesssim 2.5$. Toward higher accretion redshift ($z_{\rm acc} \gtrsim 2.5$), the thinness of substructures tends to be-

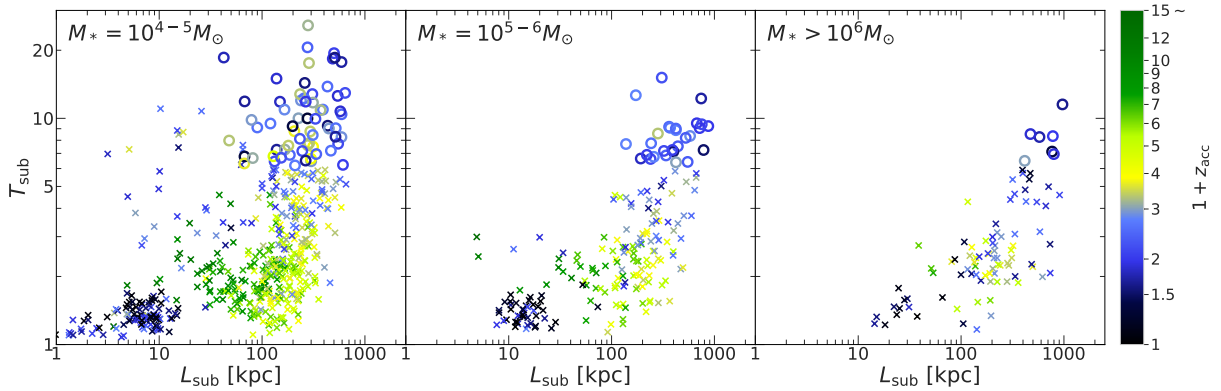

Figure 4. Distributions of length $L_{\rm sub}$ and thinness $T_{\rm sub}$ for substructures with stellar mass ranges of $M_* = 10^{4-5}, 10^{5-6}$ and $10^{6-} M_\odot$. The symbol colour gives the value of $z_{\rm acc}$. Circles denote the streams and crosses denote the others.

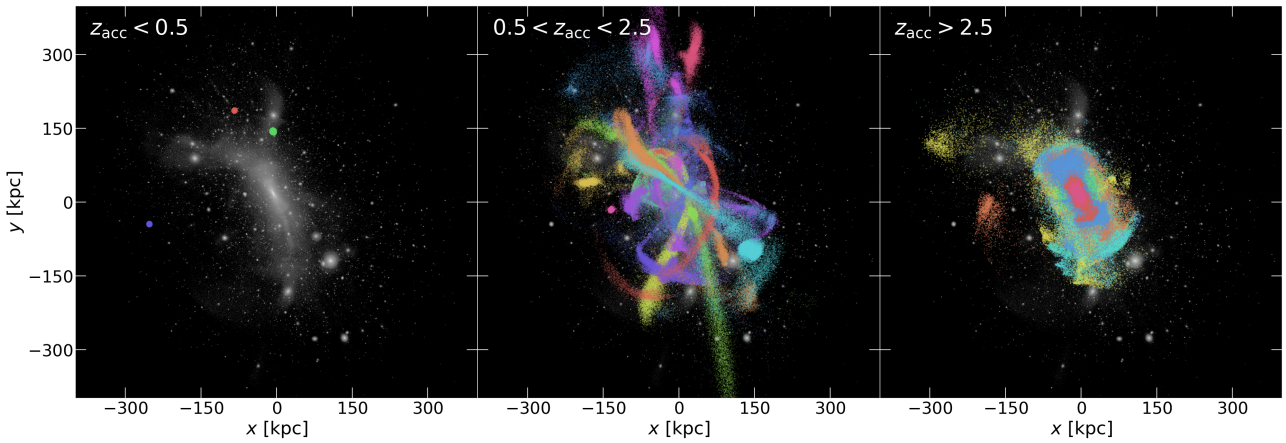

Figure 5. Distributions of stellar particles of substructures $M_* = 1 - 6 \times 10^5 M_\odot$ around a MW-sized halo (GX1) at $z = 0$. Each panel plots substructures originating in progenitors with different accretion redshift ranges of $z_{\rm acc} < 0.5, 0.5 < z_{\rm acc} < 2.5$ and $z_{\rm acc} > 2.5$. Each progenitor is visualised by different colours. The background image of each panel shows the projected dark matter density distributions within the virial radius of GX1 at $z = 0$, and the centre of each image is the centre of GX1.

come smaller due to being entirely disrupted by tidal forces, and hence they cannot be observed as streams. We have confirmed this trend in substructures with any stellar mass ranges $M_* = 10^{4-5}, 10^{5-6}$ and $10^{6-} M_\odot$.

The distributions of length and thinness of substructures also vary as pericentre $r_{\rm peri}$ and apocentre $r_{\rm apo}$ of their progenitor haloes. Substructures whose progenitor haloes experienced larger pericentre passage $r_{\rm peri} \gtrsim 100$ kpc tend to be less disrupted at $z = 0$. On the other hand, a large part of largely disrupted substructures originates in progenitor haloes with $r_{\rm peri} \lesssim 100$ kpc. Notably, substructures observed like streams tend to be concentrated in the specific range of 10 kpc $\lesssim r_{\rm peri} \lesssim 100$ kpc and 50 kpc $\lesssim r_{\rm apo} \lesssim 300$ kpc.

Throughout this paper, we do not take the effect of baryonic physics into account. Some substructures with small pericentre can be efficiently destroyed by disk shocking (e.g. D'Onghia et al. 2010; Sawala et al. 2017; Garrison-Kimmel et al. 2017; Kelley et al. 2018) and may not be observed as streams. However, in our results, streams tend to have the specific range of $r_{\rm peri} > 10$ kpc and experience a few pericentre passages after $z_{\rm acc}$ because of their specific accretion redshift range $0.5 \lesssim z_{\rm acc} \lesssim 2.5$. Therefore, baryonic physics should not strongly affect our statistical properties of streams. In the case of substructures that are strongly affected by baryonic physics, their pericentre distances must be small ($r_{\rm peri} \lesssim 10$ kpc). In addition, from Figure 4 and Figure 7, such substructures have high-$z_{\rm acc}$ and most of them are already categorised as disrupted substructures. Therefore, considering baryonic physics, these substructures may be more largely disrupted and the type of them does not change.

Although the definition of stream adopted in this study might be seemed arbitrary, there is no consensual definition of observed streams. It should be stressed that our conclusion is insensitive to the choice of the lower boundary of $T_{\rm sub}$ because the thinness of substructures varies smoothly as the orbital properties of progenitor haloes.

Our studies have been highlighting that moderate tidal effects resulted from such as specific ranges of pericentre, apocentre and $z_{\rm acc}$ of progenitor haloes are necessary to form stream-like substructures at $z = 0$. Note that we have focused on the physical origin of structural properties of substructures and have not pursued the connection with "observed" properties. This is beyond the scope of this paper and will be addressed in future studies.

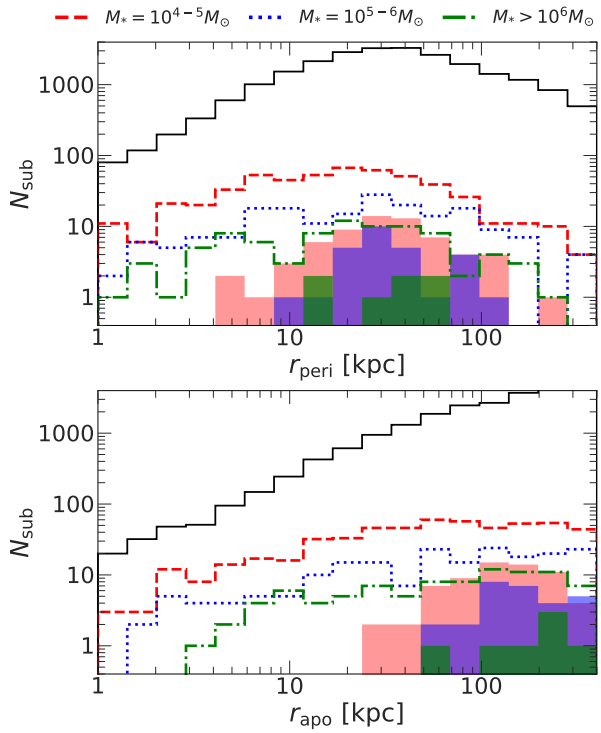

Figure 6. Distributions of pericentre $r_{\rm peri}$ (top panel) and apocentre $r_{\rm apo}$ for progenitors of substructures. Three dashed curves give the results of substructures with stellar mass ranges of $M_* = 10^{4-5}$, 10^{5-6} and $10^{6-} M_\odot$, respectively. Solid curves show the distribution of substructures with $M_{\rm vir}(z_{\rm acc}) > 10^7\ M_\odot$. The filled histograms give the distributions of the streams for the pericentre and apocentre.

ACKNOWLEDGEMENTS

We thank the anonymous referee for his/her valuable comments. We thank Miho N. Ishigaki, Kohei Hayashi and Tomoyuki Hanawa for fruitful discussions and comments. Numerical computations were partially carried out on the K computer at the RIKEN Advanced Institute for Computational Science (Proposal numbers hp150226, hp160212, hp170231, hp180180), Aterui and Aterui II supercomputer at Center for Computational Astrophysics, CfCA, of National Astronomical Observatory of Japan. This work has been supported by MEXT as "Priority Issue on Post-K computer" (Elucidation of the Fundamental Laws and Evolution of the Universe) and JICFuS. We thank the support by MEXT/JSPS KAKENHI Grant Number 17H04828, 17H01101 and 18H04337.

REFERENCES

Behroozi P. S., Wechsler R. H., Wu H.-Y., 2013, ApJ, 762, 109
Behroozi P. S., Wechsler R. H., Wu H.-Y., Busha M. T., Klypin A. A., Primack J. R., 2013, ApJ, 763, 18
Belokurov V. et al., 2007, ApJ, 658, 337
Bonaca A., Hogg D. W., 2018, ApJ, 867, 101
Boylan-Kolchin M., Besla G., Hernquist L., 2011, MNRAS, 414, 1560
Bryan G. L., Norman M. L., 1998, ApJ, 495, 80
Bullock J. S., Johnston K. V., 2005, ApJ, 635, 931
Bullock J. S., Kravtsov A. V., Weinberg D. H., 2001, ApJ, 548, 33
Busha M. T., Alvarez M. A., Wechsler R. H., Abel T., Strigari L. E., 2010, ApJ, 710, 408
Carlberg R. G., 2012, ApJ, 748, 20
Carlberg R. G., 2018a, ApJ, 861, 69
Carlberg R. G., 2018b, ArXiv e-prints
Cooper A. P., Cole S., Frenk C. S., Le Bret T., Pontzen A., 2017, MNRAS, 469, 1691
Cooper A. P. et al., 2010, MNRAS, 406, 744
Dark Energy Survey Collaboration et al., 2016, MNRAS, 460, 1270
De Lucia G., Helmi A., 2008, MNRAS, 391, 14
Diemand J., Kuhlen M., Madau P., 2007, ApJ, 667, 859
Diemand J., Madau P., Moore B., 2005, MNRAS, 364, 367
D'Onghia E., Springel V., Hernquist L., Keres D., 2010, ApJ, 709, 1138
Drlica-Wagner A. et al., 2015, ApJ, 813, 109
Dunkley J. et al., 2009, ApJS, 180, 306
Fardal M. A., Babul A., Guhathakurta P., Gilbert K. M., Dodge C., 2008, ApJ, 682, L33
Fardal M. A., Guhathakurta P., Babul A., McConnachie A. W., 2007, MNRAS, 380, 15
Fardal M. A., van der Marel R. P., Sohn S. T., del Pino Molina A., 2018, ArXiv e-prints
Fardal M. A. et al., 2013, MNRAS, 434, 2779
Foster C. et al., 2014, MNRAS, 442, 3544
Fu S. W. et al., 2018, ApJ, 866, 42
Gaia Collaboration et al., 2016, A&A, 595, A2
Garrison-Kimmel S., Bullock J. S., Boylan-Kolchin M., Bardwell E., 2017, MNRAS, 464, 3108
Gnedin N. Y., 2000, ApJ, 542, 535
Gómez F. A., Helmi A., Cooper A. P., Frenk C. S., Navarro J. F., White S. D. M., 2013, MNRAS, 436, 3602
Grillmair C. J., 2006, ApJ, 651, L29
Haiman Z., Rees M. J., Loeb A., 1997, ApJ, 476, 458
Helmi A., Babusiaux C., Koppelman H. H., Massari D., Veljanoski J., Brown A. G. A., 2018, Nature, 563, 85
Hoeft M., Yepes G., Gottlöber S., Springel V., 2006, MNRAS, 371, 401
Homma D. et al., 2016, ApJ, 832, 21
Homma D. et al., 2018, PASJ, 70, S18
Hozumi S., Burkert A., 2015, MNRAS, 446, 3100
Ibata R., Irwin M., Lewis G., Ferguson A. M. N., Tanvir N., 2001a, Nature, 412, 49
Ibata R., Lewis G. F., Irwin M., Totten E., Quinn T., 2001b, ApJ, 551, 294
Ibata R. A., Gilmore G., Irwin M. J., 1994, Nature, 370, 194
Ibata R. A., Lewis G. F., Martin N. F., 2016, ApJ, 819, 1
Ishiyama T., Enoki M., Kobayashi M. A. R., Makiya R., Nagashima M., Oogi T., 2015, PASJ, 67, 61
Ishiyama T., Sudo K., Yokoi S., Hasegawa K., Tominaga N., Susa H., 2016, ApJ, 826, 9
Johnston K. V., Bullock J. S., Sharma S., Font A., Robertson B. E., Leitner S. N., 2008, ApJ, 689, 936
Johnston K. V., Hernquist L., Bolte M., 1996, ApJ, 465, 278
Johnston K. V., Sackett P. D., Bullock J. S., 2001, ApJ, 557, 137
Johnston K. V., Zhao H., Spergel D. N., Hernquist L., 1999, ApJ, 512, L109
Kaiser N. et al., 2002, in Proc. SPIE, Vol. 4836, Survey and Other Telescope Technologies and Discoveries, Tyson J. A., Wolff S., eds., pp. 154–164
Kalirai J. S. et al., 2010, ApJ, 711, 671
Kelley T., Bullock J. S., Garrison-Kimmel S., Boylan-Kolchin M., Pawlowski M. S., Graus A. S., 2018, arXiv e-prints
Kirihara T., Miki Y., Mori M., 2017, MNRAS, 469, 3390
Kirihara T., Miki Y., Mori M., Kawaguchi T., Rich R. M., 2017, MNRAS, 464, 3509

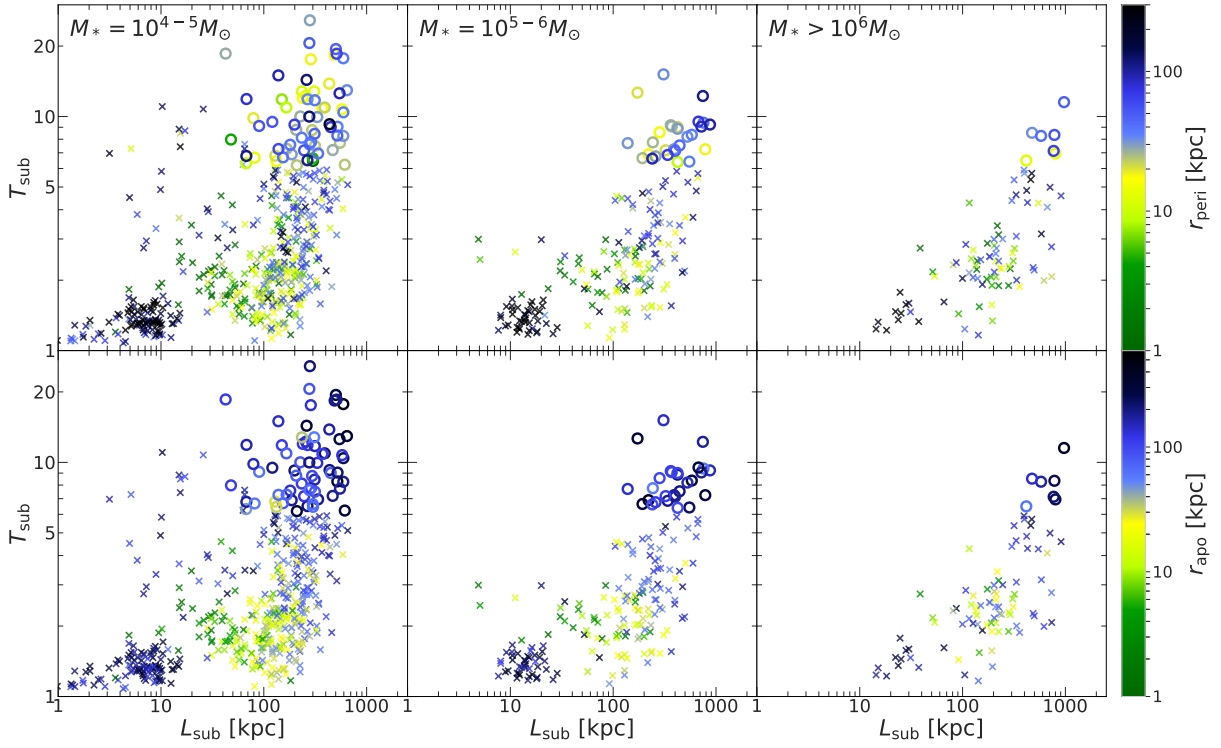

Figure 7. Distributions of length $L_{\rm sub}$ versus thinness $T_{\rm sub}$ for substructures with stellar mass ranges of $M_* = 10^{4-5}, 10^{5-6}$ and $10^{6-} M_\odot$, as functions of pericentre $r_{\rm peri}$ (upper panels) and apocentre $r_{\rm apo}$ (lower panels). Circles show streams and crosses give the others.

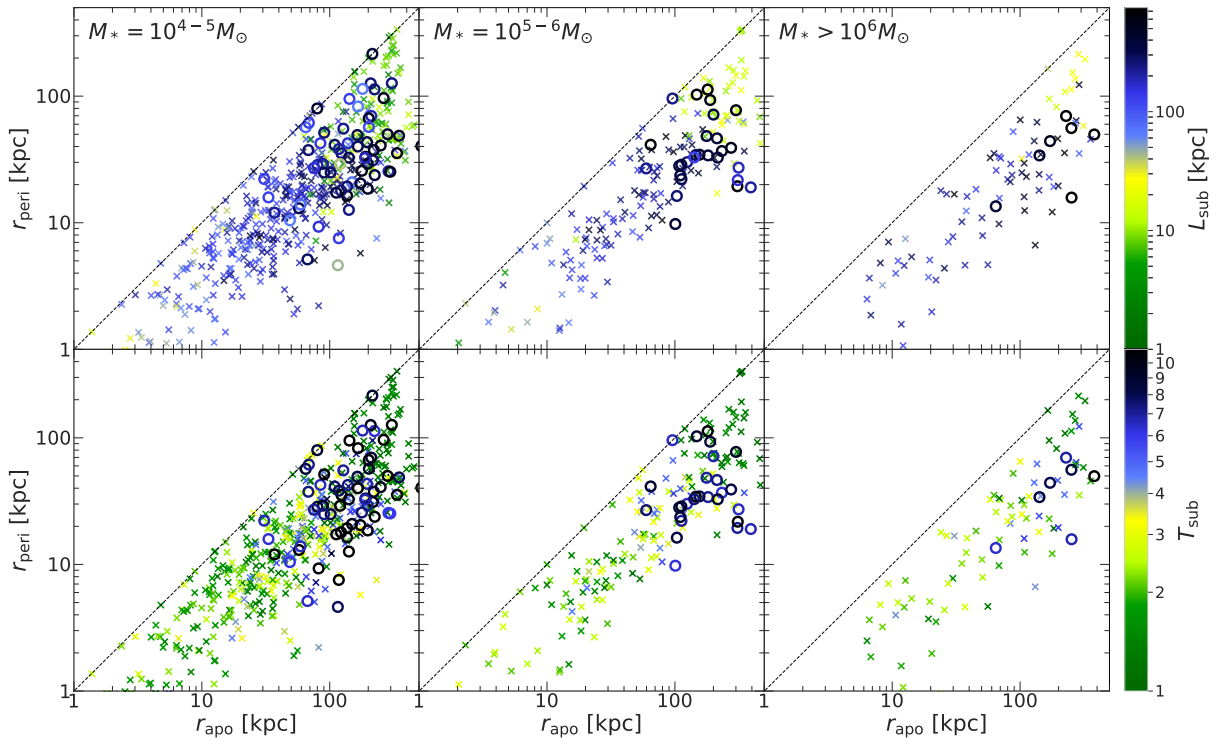

Figure 8. Distributions of pericentre $r_{\rm peri}$ versus apocentre $r_{\rm apo}$ for substructures with stellar mass ranges of $M_* = 10^{4-5}, 10^{5-6}$ and $10^{6-} M_\odot$, as functions of length $L_{\rm sub}$ (upper panels) and thinness $T_{\rm sub}$ (bottom panels). Circles show streams and crosses give the others.

Klypin A., Kravtsov A. V., Valenzuela O., Prada F., 1999, ApJ, 522, 82
Komiyama Y. et al., 2018, ApJ, 853, 29
Koposov S. E. et al., 2019, MNRAS, 485, 4726
Koposov S. E., Yoo J., Rix H.-W., Weinberg D. H., Macciò A. V., Escudé J. M., 2009, ApJ, 696, 2179
Łokas E. L., Gajda G., Kazantzidis S., 2013, MNRAS, 433, 878
Majewski S. R., Skrutskie M. F., Weinberg M. D., Ostheimer J. C., 2003, ApJ, 599, 1082
Martin N. F., Ibata R. A., McConnachie A. W., Mackey A. D., Ferguson A. M. N., Irwin M. J., Lewis G. F., Fardal M. A., 2013, ApJ, 776, 80
Martínez-Delgado D., Peñarrubia J., Gabany R. J., Trujillo I., Majewski S. R., Pohlen M., 2008, ApJ, 689, 184
McConnachie A. W., 2012, AJ, 144, 4
McConnachie A. W. et al., 2009, Nature, 461, 66
Miki Y., Mori M., Kawaguchi T., Saito Y., 2014, ApJ, 783, 87
Miki Y., Mori M., Rich R. M., 2016, ApJ, 827, 82
Miyazaki S. et al., 2006, in Proc. SPIE, Vol. 6269, Society of Photo-Optical Instrumentation Engineers (SPIE) Conference Series, p. 62690B
Miyazaki S. et al., 2012, in Proc. SPIE, Vol. 8446, Ground-based and Airborne Instrumentation for Astronomy IV, p. 84460Z
Moore B., Ghigna S., Governato F., Lake G., Quinn T., Stadel J., Tozzi P., 1999, ApJ, 524, L19
Okamoto T., Gao L., Theuns T., 2008, MNRAS, 390, 920
Peñarrubia J., Belokurov V., Evans N. W., Martínez-Delgado D., Gilmore G., Irwin M., Niederste-Ostholt M., Zucker D. B., 2010, MNRAS, 408, L26
Peñarrubia J., McConnachie A., Babul A., 2006, ApJ, 650, L33
Planck Collaboration et al., 2014, A&A, 571, A16
Planck Collaboration et al., 2018, ArXiv e-prints
Richardson J. C. et al., 2011, ApJ, 732, 76
Sales L. V. et al., 2008, MNRAS, 389, 1391
Sales L. V., Navarro J. F., Abadi M. G., Steinmetz M., 2007, MNRAS, 379, 1464
Sandford E., Küpper A. H. W., Johnston K. V., Diemand J., 2017, MNRAS, 470, 522
Sawala T., Pihajoki P., Johansson P. H., Frenk C. S., Navarro J. F., Oman K. A., White S. D. M., 2017, MNRAS, 467, 4383
Shipp N. et al., 2018, ApJ, 862, 114
Simon J. D., 2018, ApJ, 863, 89
Tollerud E. J. et al., 2012, ApJ, 752, 45
Varghese A., Ibata R., Lewis G. F., 2011, MNRAS, 417, 198
Warnick K., Knebe A., Power C., 2008, MNRAS, 385, 1859
Wetzel A. R., 2011, MNRAS, 412, 49
White S. D. M., Rees M. J., 1978, MNRAS, 183, 341

APPENDIX A: COMPARING STRUCTURAL PROPERTIES WITH DIFFERENT MOST-BOUND FRACTION $f_{\rm MB}$ FOR THE PARTICLE TAGGING METHOD

We compare statistics in structural properties of substructures using three most-bound fraction $f_{\rm MB} = 0.05, 0.10$ and 0.20 for the Particle Tagging method. The most-bound fraction $f_{\rm MB}$ is a free-parameter, which determines the fraction of stellar particles to dark matter particles of a progenitor halo at the accretion redshift $z_{\rm acc}$. Therefore, the number of stellar particles in haloes increases with increasing $f_{\rm MB}$. The detail is given in Section 3.1.

Figure A1 is the same as Figure 4. However, top, middle and bottom panels show the distributions of length and thinness of substructures at $z = 0$ for $f_{\rm MB} = 0.05$, 0.10 and 0.20, respectively. The distributions of the length tend to become slightly longer with increasing $f_{\rm MB}$. It is expected that tidal stripping preferentially occurs in the outer part of subhaloes, and hence the stellar particles of substructures are more vastly scattered in the model using greater $f_{\rm MB}$. However, overall distributions of length and thinness are not so changed regardless of the adopted $f_{\rm MB}$. Especially, for largely disrupted substructures with $L_{\rm sub} \gtrsim 10$ kpc, their length and thinness vary smoothly as $z_{\rm acc}$ for any given $f_{\rm MB}$. For less disrupted substructures with $L_{\rm sub} < 10$ kpc and $T_{\rm sub} \sim 1$, their number with $z_{\rm acc} \gtrsim 0.5$ increases with decreasing $f_{\rm MB}$, especially in the low stellar mass range of $M_* = 10^{4-5} M_\odot$. This is because that stellar components tagged with smaller $f_{\rm MB}$ are more tightly bound and less affected by tidal interactions with host haloes.

From these results, we can conclude that our statistical results of the relationship between the structural properties of substructures and the orbits of their progenitors are insensitive to the choice of $f_{\rm MB}$.

APPENDIX B: COMPARING STRUCTURAL PROPERTIES WITH DIFFERENT THRESHOLD $\rho_{N_{\rm p}}$ FOR OUTLIER REMOVAL STEP OF QUANTIFYING $L_{\rm sub}$

We compare statistics in structural properties of substructures using three thresholds $\rho_{N_{\rm p}} = 0, 5$ and 25 for outlier removal step of quantifying length of substructures. The definition of the threshold $\rho_{N_{\rm p}}$ is described in Section 3.4.1.

Figure B1 is the same as Figure 4. However top, middle and bottom panels show the distributions of length and thinness of substructures at $z = 0$ for $\rho_{N_{\rm p}} = 0, 5$ and 25, respectively. The distributions of length tend to become slightly shorter with increasing $\rho_{N_{\rm p}}$, however, overall trends of the distributions are not changed in any $\rho_{N_{\rm p}}$. Therefore, we conclude that our statistical results of the structural properties of substructures are insensitive to the choice of $\rho_{N_{\rm p}}$.

This paper has been typeset from a TEX/LATEX file prepared by the author.

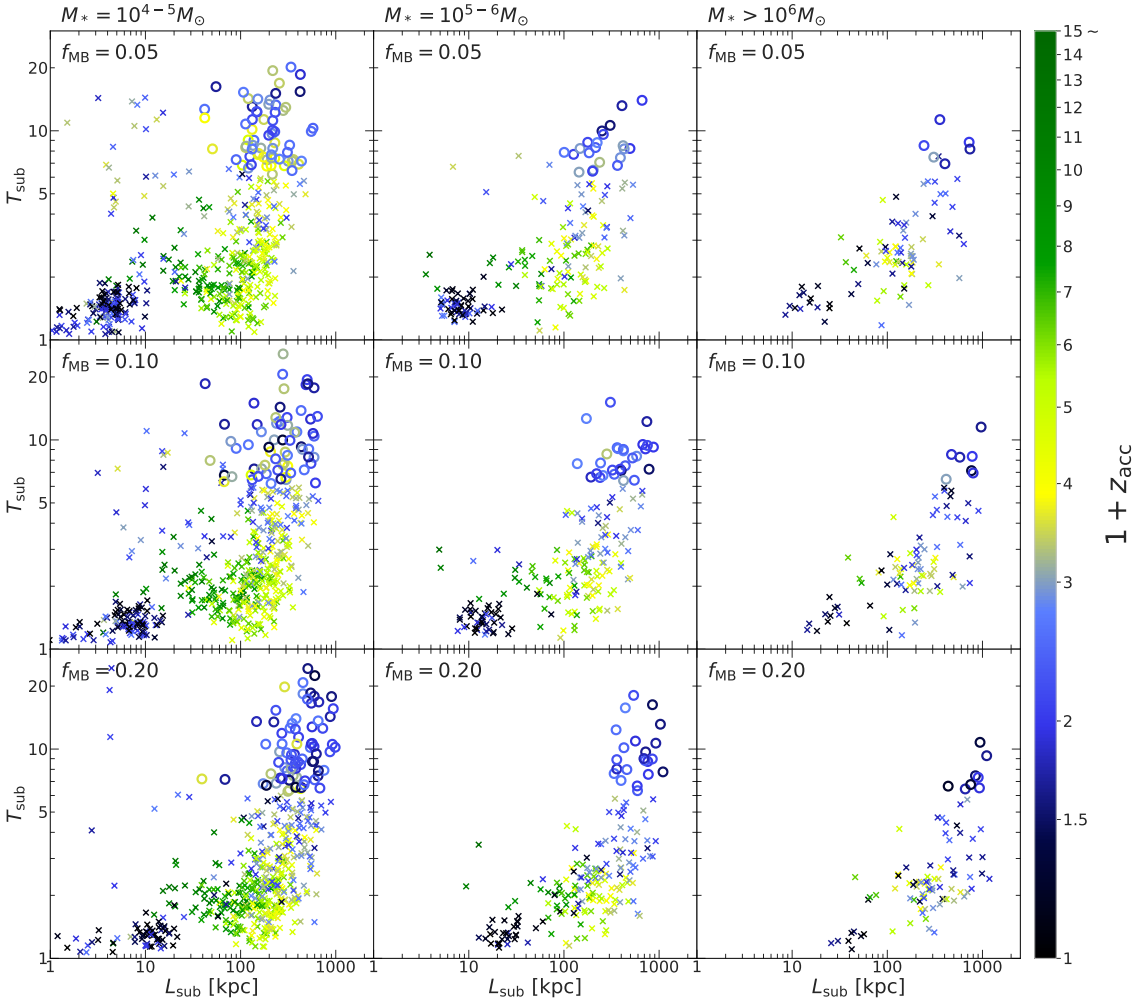

Figure A1. Same as Figure 4. Top, middle and bottom panels show the distributions of length and thinness of substructures at $z = 0$ for $f_{\rm MB} = 0.05$, 0.1 and 0.2, respectively.

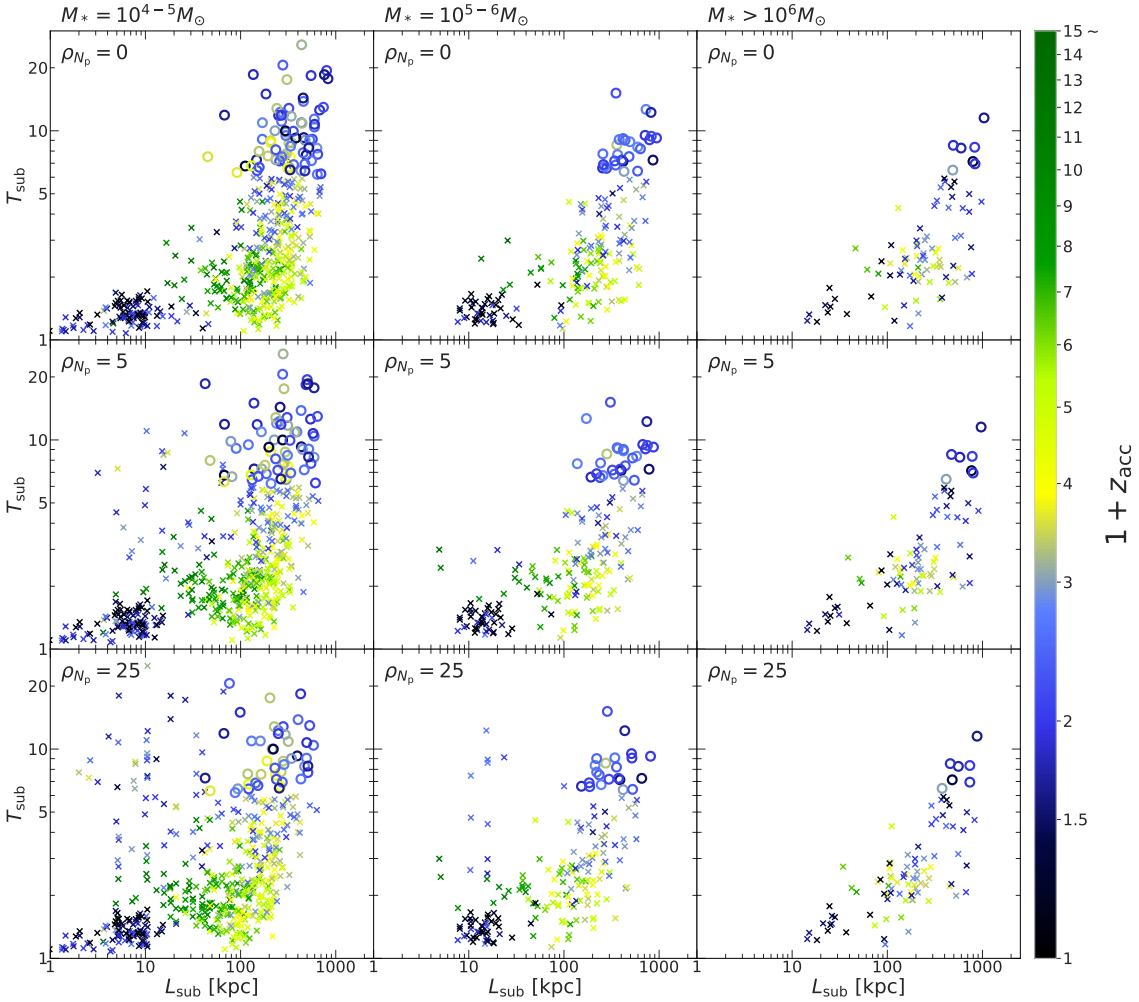

Figure B1. Same as Figure 4. Top, middle and bottom panels show the distributions of length and thinness of substructures at $z = 0$ for $\rho_{N_p} = 0, 5$ and 25, respectively.